Ultra-thin electrospun nanofibers for development of damage-tolerant composite laminates

Article *in* Materials today: proceedings · November 2019

DOI: 10.1016/j.mtchem.2019.100202

7 authors, including:

Donglan An
Cranfield University
2 PUBLICATIONS **3** CITATIONS
SEE PROFILE

Saeid Lotfian
University of Strathclyde
16 PUBLICATIONS **167** CITATIONS
SEE PROFILE

Daria Mesbah
Aero Gearbox International
2 PUBLICATIONS **3** CITATIONS
SEE PROFILE

David Ayre
Cranfield University
20 PUBLICATIONS **125** CITATIONS
SEE PROFILE

Contents lists available at ScienceDirect

Materials Today Chemistry

journal homepage: http://ees.elsevier.com

Ultra-thin electrospun nanofibers for development of damage-tolerant composite laminates

D. An [a], S. Lotfian [b], D. Mesbah [a], D. Ayre [a], A. Yoosefinejad [c], V.K. Thakur [a,d,*], H. Yazdani Nezhad [a,**]

[a] Enhanced Composites & Structures Centre, School of Aerospace, Transport and Manufacturing, Cranfield University, MK43 0AL, UK
[b] Offshore Engineering Institute, University of Strathclyde, G1 1XQ, UK
[c] Munro Technology Limited, Lufton Height Commerce Park, Yeovil, BA22 8UY, UK
[d] Department of Mechanical Engineering, School of Engineering, Shiv Nadar University, Uttar Pradesh, 201314, India

ARTICLE INFO

Article history:
Received 23 July 2019
Received in revised form 4 September 2019
Accepted 24 September 2019
Available online xxx

Keywords
Electrospinnig; Nanofibers
Polymer matrix composite
Fracture toughness
Chemical bonding
Nanofiber deformation

ABSTRACT

The present article overcomes existing challenges in inter-laminar toughening of novel multifunctional fiber-reinforced polymer composites via development and embedment of highly stretched, ultra-thin electrospun thermoplastic nanofibers made of polyamide 6.6. The nanofibers exhibit significant enhancement of the composite laminate's structural integrity with almost zero weight penalty via ensuring a smooth stress transfer throughout the plies and serving tailoring mechanical properties in desired directions, with no interference with geometric features, e.g., thickness. The findings for 1.5 g per square meter electrospun nanofibers have demonstrated, on test coupon specimens, improvements up to 85% and 43% in peak load and crack opening displacement, respectively, with significant improvement (>25%) and no sacrifice of fracture toughness at both initiation and propagation phases. The initial stiffness for the modified specimens was improved by nearly 150%. The enhancement is mainly due to nanofibers contributing to the stiffness of the resin-rich area at the crack tip adjacent to the polytetrafluoroethylene (PTFE) film. Glass fiber-reinforced woven phenolic pre-impregnated composite plies have been modified with the nanofibers (each layer having an average thickness of <1 micron) at 0.5, 1.0, 1.5, 2.0 and 4.0 gsm, electrospun at room temperature on each ply, and manufactured via an autoclave vacuum bagging process. Inter-laminar fracture toughness specimens were manufactured for Mode I (double cantilever beam) fracture tests. It was found that there is threshold for electrospun nanofibers density, at which an optimum performance is reached in modified composite laminates. The threshold is influenced by the plastic deformation mechanism at the crack tip, the fiber bridging between the adjacent plies afforded by the nanofibers, and the density of the electrospun fibers. Such optimum performance was found linked to the nanofibers at a specific density. Excessively increasing above the threshold (herein >2.0 gsm) degrades the adhesion properties (chemical bonding) between glass fibers and the phenolic matrix. The density of nanofibers increases, so does the likelihood of forming a physical barrier between the plies resulting in the loss of resin flow and poor adhesion. Such an effect was evident from microscopic investigations and reduction in fracture toughness data at the initiation and propagation phases.

1. Introduction

Fiber-reinforced polymer composite materials are extensively used in aerospace and general transport owing to their high mechanical properties, low density, and tailorability to align with a broad and diverse range of applications. Polymer matrix composites (PMCs) present excellent specific stiffness and strength which result in dramatic weight reduction in the design. The use of PMCs on transport structures enables substantial fuel efficiency, and therefore has a direct impact on CO_2 emission reduction. However, one of the principal limitations of PMCs is the low damage tolerance of these materials and consequently a short lifetime. In particular, the delamination growth between reinforcing plies in PMC laminates is considered one of the most predominant and life-limiting type of damage encountered in composite laminates during service that can be detrimental to flight safety [1–6]. Furthermore, whereas impact or dynamic events can significantly reduce mechanical properties, impact-induced delamination damage is hardly detectable by the existing non-destructive inspection (NDI) techniques [7–9]. Of the total composite damage, 87% is caused by impact with energies ranging from 5 to 100 joules, known as low-velocity (energy) impacts [4–6,10]. In such terms, several different methods have been developed to toughen composite materials to resist inter-laminar

* Corresponding author.
** Corresponding author.
E-mail addresses: Vijay.kumar@cranfield.ac.uk (V.K. Thakur); h.yazdani-nezhad@cranfield.ac.uk (H. Yazdani Nezhad)

https://doi.org/10.1016/j.mtchem.2019.100202
2468-5194/

delamination [3,11]. These delamination mechanisms are often driven by instantaneous development of interfacial cracks between two neighboring plies. The crack propagation may be quantified by the strain energy release rate (G), which is the amount of energy needed to create a crack surface (J/m^2), also known as the delamination toughness between two plies, therefore, a function of crack face initiation and propagation. Its value can vary depending on the crack length and strengthening mechanisms such as adhesion between the plies, between reinforcements and polymers, and fiber bridging [3,11] where reinforcements (e.g., carbon, glass, or polymeric fibers) bridge across the faces of the neighboring plies.

Prevention of the occurrence of delamination has to be taken into account during the design and conception of composite laminates, sources of out-of-plane stressing often being caused by load-path discontinuity. Another source is manufacturing-induced defects as well as impact-induced damage that cannot be entirely avoided [12–16] such as kissing bonds representative of pre-existing poor adhesion properties. Thus, increasing the intrinsic fracture toughness of composite laminates is crucial. Interleaving techniques have been developed via inserting inter-laminar layers, for example, poly-ether-imide veils [17], for improving toughness between the original composite plies. This method is effective as it enables impact damage absorption and hinders the damage at its initial stage; however, these inserted layers are also relatively heavy and thick (the thickness is almost the same as the original composite ply, e.g., ~250 microns) and, therefore, reduce the specific stiffness and specific strength of the laminates [17].

When many successive plies have the same orientation, the remaining mismatched interfaces will suffer from extensive damage, and the laminate damage resistance is reduced, whereas increasing the number of dissimilar interfaces increases the energy absorbed during delamination [18]. It means that thicker plies would have fewer interfaces for the same structure's width that leads to relatively low strain energy absorption during delamination.

Interleaving techniques have shown encouraging results in terms of the laminate's fracture toughness enhancement [19–27]. To tackle its main drawback, the weight penalty in addition to thickness and geometry interference, researchers have studied the possibility to introduce a light layer of thermoplastic electrospun nanofibers, which often enable multifunctionality such as that in polyvinylidene fluoride (PVDF) materials, e.g., enabling piezo-electricity and energy harvesting [19–27]. Electrospinning is an established and scalable technique to generate continuous fibers at the nanoscale, with a broad range of constituents. The fibers are produced from a polymeric solution, stretched by the electrostatic repulsion between surface charges at relatively high voltages and the evaporation of solvent [28–30]. In particular, interfacial toughening based on thermoplastic nanofibers electrospun from thermoplastics gains an increasing interest [31–41]. The advantage of this approach is that there is almost zero thickness or weight penalty (<0.2%), because the nanofibrous layer is in the order of 100 nm thinness, and is highly localized between the plies, leading to only marginal loss of in-plane properties. The nanofiber fabrication is cost efficient and rapid, and the existing composite processes do not have to be changed to meet the requirement of such a toughening technique. Though the toughening process is efficient and straightforward, there is a research gap to address the drawbacks of not having sufficient adhesion properties between PMC plies and the thermoplastic nanofibers. If the electrospinning density is not controlled properly, the modified laminate may re-possess interlayer defects because of the presence of nanofibers rather than chemical bonding, ductility, and plasticity improvement between plies.

The aim of this study is to develop a modified PMC laminate with zero weight and thickness penalty and quantify the effect of embedment of nanofibers on the fracture toughness of composite laminates made of glass fiber-reinforced PMC composites, at different nanofiber layer thicknesses and aerial densities, gsm.

2. Materials and manufacturing

The PMC pre-pregs used in this study were phenolic-based glass fiber-reinforced composite laminates made of 16 plies of intermediate modulus, 0.25 mm-thickness woven glass fiber composite pre-pregs having a density of 2039 kg/m^3, manufactured by BRP Composites Ltd. In a quasi-isotropic symmetric stacking sequence ($[45/0/90/45/0/90/45/0]_S$), the composite exhibited Young's modulus of E_{11} = 22.9 GPa, E_{22} = 21.6 GPa, and E_{33} = 3.8 GPa, respectively, in longitudinal, lateral, and through-thickness directions, failing at approximately 2% glass fiber strain based on our primary investigations [21].

The inter-laminar toughening nanofibers were thermoplastic nylon-6,6 produced by a high voltage, room temperature electrospinning technique at Munro Technology Limited. The process enabled stretching of the polymer up to 500%. There is no additional mechanical stretching involved in the electrospinning, and therefore the nanofibers stretched because of the electrospinning process.

The nylon-6,6 powder sample exhibited a homogeneous sphere size with an average diameter of approximately 100 μm, as shown in Fig. 1(a). The powders' electrospun nanofibers up to 300% stretching resulted in the formation of nanofiber bundles as shown in Fig. 1(b), comprising nanofibers with diameters ranging from 400 nm to 3 microns. Further stretching (up to 500%) led to much smaller diameters (~100 nm) and more consistent range of diameters, as shown in Fig. 2.

The composition of the powder and nanofibers (taken from the surface of four randomly selected nanofibers) was obtained using energy dispersive X-ray spectroscopy (EDS), and is tabulated in Table 1.

The EDS data—performed multiple times per sample to generate a robust statistical distribution—for the powder and electrospun nanofiber bundles were compared. The results for the powder

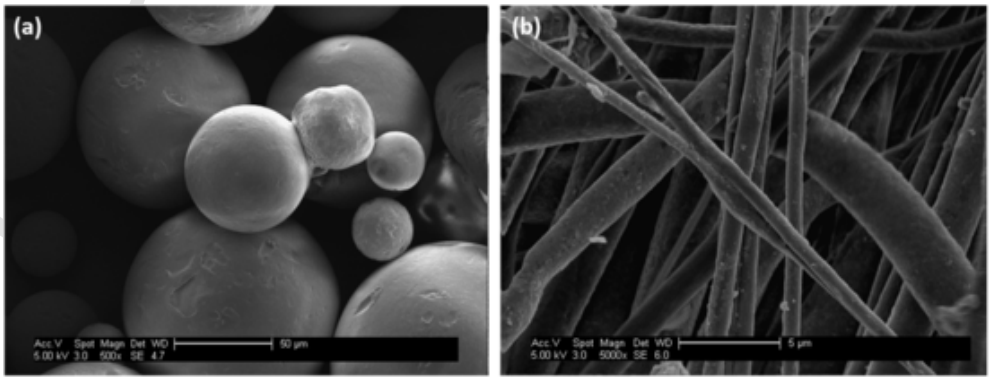

Fig. 1. Comparison of morphology of (a) nylon-6,6 powder and (b) electrospun nanofibers, stretched up to 300%.

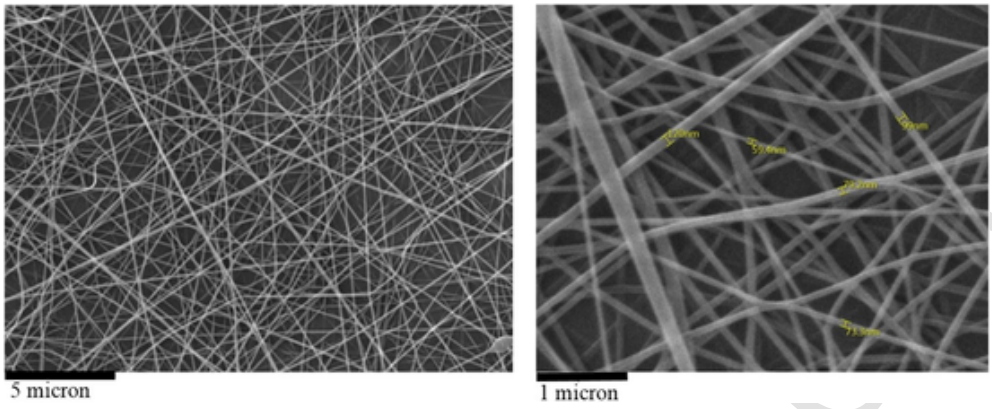

Fig. 2. Nylon-6,6 nanofibers electrospun, stretched up to 500%, and deposited directly over the phenolic composite plies at densities of 2.0 gsm and 5.0 gsm.

Table 1
EDS data from surfaces of electrospun nanofibers.

Spectrum Label	C (%)	N (%)	O (%)	F (%)	Al (%)	Si (%)	Ca (%)
Spectrum 1	28.77	3.85	36.74	0.04	4.4	12.59	13.61
Spectrum 2	41.23	9.21	25.03	0	1.03	19.88	3.62
Spectrum 3	35.65	3.34	26.66	0.35	1.21	29.7	3.09
Spectrum 4	50.2	12.48	21.17	0.5	0.32	14.59	0.74

indicated a carbon:fluorine ratio of between 4:1 and 2:1, indicating significant sample carbon-based contamination, as the expected result was a 1:1 ratio of carbon to fluorine (PVDF unit cell is $–C_2F_2H_2–$). The contamination is attributed to carbon arising from the manufacturing process, manipulation, and detection of the carbon tape on which the sample is stuck for being analyzed. As no sample exceeded a fluorine ratio of 50%, it can be assumed that this is an accurate assumption. No peak that could be attributed to any other atomic element than carbon, fluorine, or gold (coating) was identified. In particular, no nitrogen was observed in any of the spectrums of the prepared fibers, indicating that a negligible amount of solvent was present.

Fourier transform infra-red (FTIR) spectroscopy was carried out on the powder and the electrospun nanofiber bundles at different stretching up to 500%. Fig. 3 compares the FTIR-ATR (attenuated total reflection) ZnSe spectrums for the samples with most of the peaks between 550 cm^{-1} and 1450 cm^{-1} (below 550 cm^{-1}, the quality of the measurement was too dependent on the setup device and therefore makes it unreliable, and above 1450 cm^{-1}, all spectrums were flat with limited peaks).

It can be observed that the trend in the appearance of the peaks is almost identical for the spectrums. However, the powder spectrum is slightly different from the others, with some peak shifts (at 870, 1070, or 1180 cm^{-1}) and higher additional peaks at approximately 612, 760, 795, 1207, or 1384 cm^{-1}. This is because the powder was the raw material and has not been stretched unlike the other samples.

Finally, the nanofibers with the average diameter of 100 nm (stretched up to 500%) were directly electrospun on the surface of each ply as shown in Fig. 2 to create the modified composite pre-pregs. The pore size distribution of the electrospun mats of different density is a critical parameter affecting the fracture energy and toughening mechanisms. The nanofiber mat thickness was controlled via controlling the speed of electrospinning with respect to the pre-preg surface in a way to freely embed over the surface and avoid further stretching. Thereby, it was ensured that the nanofibers mat thickness was nearly identical to the average diameter of the nanofibers.

Dynamic mechanical analysis (DMA) measurements were also carried out on the pristine and nanofiber-modified pre-preg plies to identify any possible variation in curing parameters needed for the co-process. The results presented in Fig. 4 show a slight effect of nano-modification on glass temperature with maximum 30% increase in tan(δ) data.

To prepare the test specimens, the pre-preg lamina was cut into plies. For the plies oriented at −45° or +45°, panels of 550 mm × 424 mm dimensions were cut. Plies were carefully

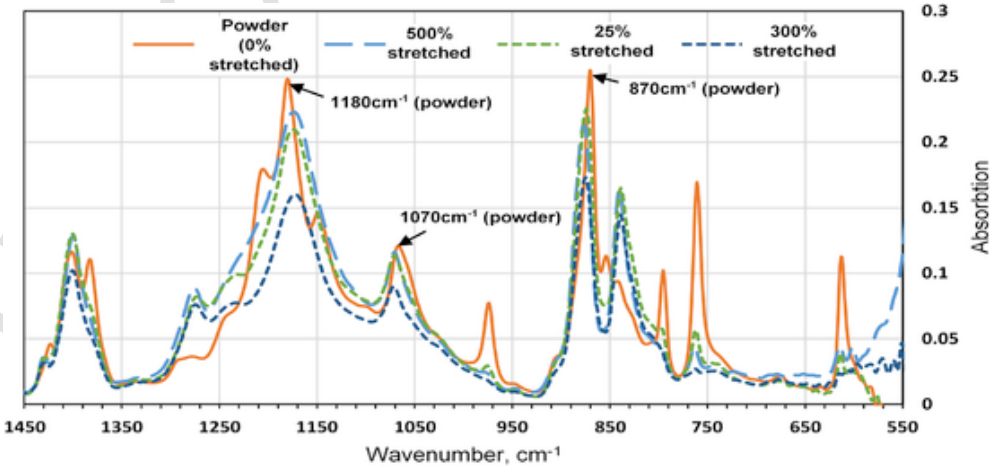

Fig. 3. Comparison of FTIR spectrums for the powder and nanofibers, ranged from 550 cm^{-1} to 1450 cm^{-1}.

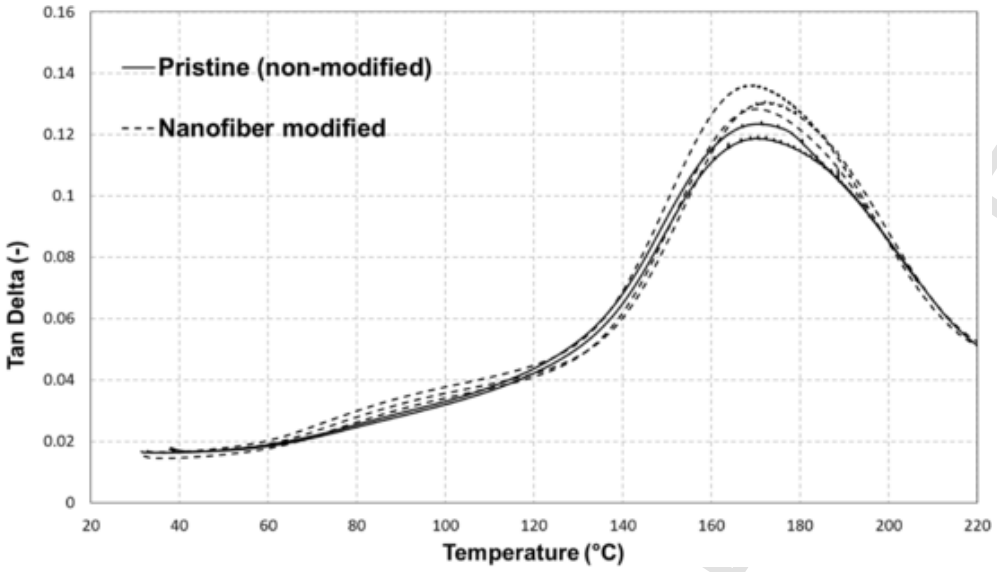

Fig. 4. Effect of electrospun nanofibers on the glass transition temperature (DMA data) showing approximately identical temperature of 170 °C.

stacked and the waxed paper protecting the nanofibers was released in a protective environment just before laying up over the middle ply, to avoid moisture absorption. Post laying-up, the specimens were cured using vacuum bagging in an autoclave under a pressure of 6 bar and at 125 °C for 2 h, with an initial heating rate of 1 °C/min. Specimens were then cut to produce Mode I fracture toughness test specimens according to ASTM D5528 [42] with $a_0/W = 50/125 = 0.4$. A non-adhering release film, made of PTFE in thickness of 15 micron, was inserted over the mid-plane plies, on both panels to mimic a pre-existing crack length of approximately 50 mm. Thus, the plies adjacent to this insert were not bonded post curing. This way, the insert simulated a stress concentration site to produce fracture test specimens in opening mode, double cantilever beam (DCB) specimens. End blocks were manufactured to adhesively tab the specimens for Mode I testing as shown in Fig. 5.

3. Experiments

3.1. Fracture toughness specimens and tests

Fracture toughness specimens for Mode I testing (opening mode) followed the ASTM D5528 standard's specifications [42] using the DCB specimens in 20 mm × 125 mm dimensions, presented in Fig. 5 for unloaded and loaded conditions. Edge-side release films were embedded onto the DCB specimens over the mid-ply to create pre-existing crack faces before the materials were co-processed. Four specimens per category were manufactured to examine the repeatability of the test data. Pristine reference specimens were also manufactured for testing to create a baseline for comparative studies. The same manufacturing protocol as that for the nanofiber-modified samples was used (outlined in Section 2) to manufacture the pristine reference samples using the autoclave under 6 bar pressure and at 125 °C for 2 h with the heating rate of 1 °C/min.

Fracture toughness tests were performed using a Zwick 10 kN force machine equipped with a load cell of 2.0 kN. The crosshead opening displacement speed for all the tests was set to be at or below 1 mm/min to ensure quasi-static loading condition. Great care was taken to avoid initial loading on the pre-existing crack and the nanofiber layers when fitting the load blocks on the jigs, to verify the pins inserted in the blocks were parallel, and to avoid torsional moment. Load and displacement data were recorded using the testXpert v5.01 software on a desktop computer. In both testing, the delaminated crack length measurement was carried out using continuous visual observations from one side of the specimens, Fig. 5, via an optical magnifier. The load levels were automatically recorded against the crack growth data.

Mode I fracture toughness (G_I) was then evaluated based on the modified beam theory (Eq. (1)) to account for end blocks and large deformation conditions as the specimens' crack were allowed to

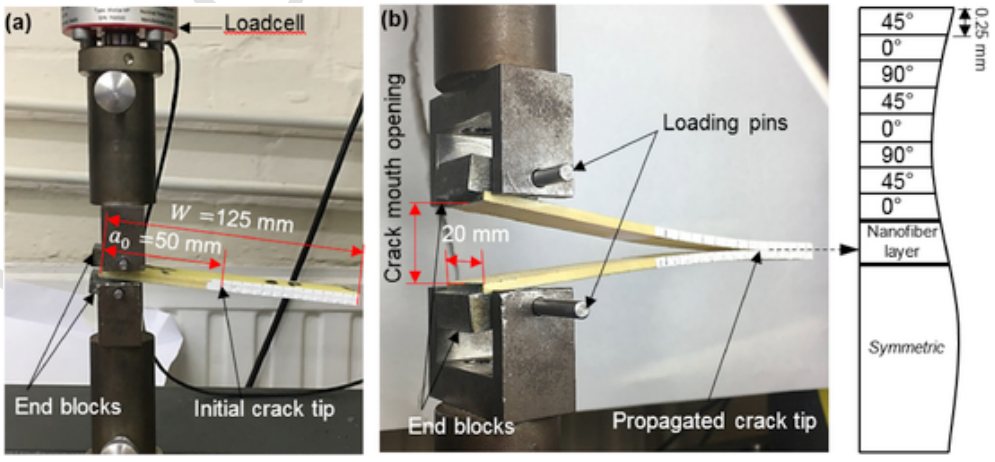

Fig. 5. Mode-I DCB specimen test setup demonstrating the composite specimen with the white-painted edge marked up at every millimeter for crack propagation studies.

propagate longer than the minimum required. The distance between the loading pin hole and the front of the tab was 4 mm, and that between the hole and the surface of the DCB specimen was approximately 3.5 mm. Such values were taken into account for theoretical corrections of the G_I values given by:

$$G_I = \frac{3P\delta}{2b\,(a+\Delta)} \times \frac{F}{N} \tag{1}$$

where P is the applied load, δ is the load point displacement measured using the machine head's linear variable differential transformer, b is the specimen's width, and a is the delamination crack length measured optically. Δ is the correction factor that accounts for the fact that opening DCB is not a perfect cantilever with its end totally fixed. It is determined experimentally by generating a least squared plot of the cube root of compliance, $C^{1/3}$ where $C = \delta/P$, as a function of delamination length. The large deformation factor, F in Eq. (1), corrects the fact that as the angle of the end blocks changes during loading, their orientation also changes that influences the distance between the crack front and the loading pin. The use of end blocks, which can cause a stiffening effect of the specimen arms or different displacement relative to the ideal loading point, is corrected by the N factor. Values for F and N are given by:

$$F = 1 - \frac{3}{10}\left(\frac{\delta}{a}\right)^2 - \frac{2}{3}\left(\frac{\delta l_1}{a^2}\right) \tag{2}$$

$$N = 1 - \left(\frac{l_2}{a}\right)^3 - \frac{9}{8}\left[1 - \left(\frac{l_2}{a}\right)^2\right]\left(\frac{\delta l_1}{a^2}\right) - \frac{9}{35}\left(\frac{\delta}{a}\right)^2 \tag{3}$$

where l_2 is the horizontal distance between the load pin's center and the end side of loading block, and l_1 is the distances from the center of loading pin to mid-plane of the specimen and to the edge of the loading blocks, respectively.

The initial fracture toughness in opening mode, $G_{I,ini}$, is calculated based on the standard's recommendation, and is given by:

$$G_{I,ini} = \frac{3P\delta}{2ba} \tag{4}$$

3.2. Microscopy

Optical microscopy and scanning electron microscopy (SEM) were used to identify damage mechanisms that occurred in the specimens post fracture toughness testing. The specimens for SEM were plasma coated with a thin gold layer, ~15 nm thickness at 20 mA, to improve the imaging of the polymers via discharging surface electrons.

4. Results and discussion

Raw data of applied force are plotted against crack mouth opening displacement in Fig. 6 for all the modified phenolic composite DCB specimens. The data shown in all sub-figures for the modified specimens (dashed lines) are compared with those of the pristine specimens (solid lines).

All DCB specimens, whether with (modified) and without (pristine) nanofibers, have the same physical dimensions and same initial crack lengths of 50 mm; however, the initial stiffness values of the four pristine specimens vary substantially (>50%). The same disparity is seen for the modified specimens with densities of 1.0 gsm and 5.0 gsm, Fig. 6(b) and (e). Such disparity rises for both pristine and modified specimens.

The PTFE tape was inserted to simulate a pre-existing crack and, therefore, had no influence in driving the initial stiffness, i.e., before crack initiation. The panels from which the specimens were extracted, however, showed a different quality post process, in different locations, apparently a sign of non-uniform cure at the center and the edge sides due to non-uniform heat transfer in the conventional oven. As the panels were sufficiently large, the specimens cut near the edge of the panels are believed to attain a different quality, which may have led to the disparity in the initial stiffness data. However, it is acknowledged that non-uniform cure in relatively large panels in actual applications is a common challenge especially in non-flat panels with back structures.

As seen, in comparison with the pristine data, the peak load increases with the increasing nanofiber density from 0.5 to 2.0 gsm (Fig. 6(a)–(d)) and decreases for densities >2.0 gsm (Fig. 6(e)), as also observed for the increasing displacement data (x-axis).

Fig. 7 suggests that the 1.5 gsm modified composite exhibits a better performance with 85% improvement in the peak load (=100 × (48 N–26 N)/26 N) while having the lowest disparity (scatter in data), a sign of robust reliability based on repeatable test data. Moreover, before any crack initiation, the initial stiffness of the modified composite has significantly been improved at 1.5 and 2.0 gsm with nearly 145% and 110% improvements, respectively. Such an increase in the opening stiffness before crack is initiated suggests a high modulus compared to that of the pristine specimen within the elastic regime, attributed to high adhesion properties (e.g., interfacial strength) in the opening mode.

The maximum force and opening displacement data extracted from Fig. 6 and averaged data of the four specimens are presented in Fig. 7. As seen, the peak load for the 1.0 gsm reached a high value of 52 N for one specimen whereas the other specimens' data suggest slightly lower levels than those of the pristine samples (Figs. 6(b) and 5(a) showing high-scattered data as a result of such high disparity).

As seen in Fig. 6, the significant stiffening occurs only at 1.5 gsm and 2.0 gsm (Fig. 6 (c, d)). Taking the 1.5 gsm as an example, this is in a consistent trend with the improvements in the peak load by 85% and the maximum displacement by 43%. As the stiffness is the ratio of force over displacement, the stiffness for 1.5 gsm is almost doubled, by ~198% (=85/43). It may be noted that this occurs in the linear elastic regime where mainly deformation mechanisms are in play, rather than damage. The authors have observed that in such elasticity improvement scenarios, two microstructural mechanisms are prevailing for the 1.5 gsm and 2.0 gsm which are rarely observed in other density levels: adhesion of nanofiber layers to the polymer (and in some cases to fibers) and intact fiber bridging, also consistent with the initiation of crack surfaces which requires 25% higher energy to initiate a fracture (such as that in Fig. 8(a)), meaning that the energy dissipated initially by the existing deformation mechanisms in the cases of 1.5 gsm and 2.0 gsm prior to damage.

The fracture toughness data based on the measurement of crack length in opening mode are given in Eq. (1) for propagation and Eq. (4) for initiation phases, and are plotted in Fig. 8 as a function of the increasing nanofiber density (0.5 gsm to 4.0 gsm). As seen, the fracture responses at both initiation and propagation phases have improved for the 1.5 gsm specimens by more than 25% compared to those of the pristine samples. Such improvement may seem trivial compared to the existing interleaving veils; however, it should be noted that the 25% improvement is obtained at the zero weight and thickness penalty, and in laboratory-scale specimens. Scale-up analysis for large structural scale components in actual applications requires further investigation. The initiation fracture toughness is slightly higher than the propagation one almost for all cases, due to the nanofibers-induced crack tip being blunt shape rather than sharp and straight. The fiber bridging was evident during fracture toughness testing of 1.5 and 2.0 gsm specimens, significantly occurring due to the nylon nanofibers sticking to the glass fiber and the phenolic matrix. This has contributed to hindering instantaneous separation via introducing plasticity mechanisms surrounding the crack tip edges, as postulated in Ref. [15]. Consequently, the G_I value increased during the propagation phase.

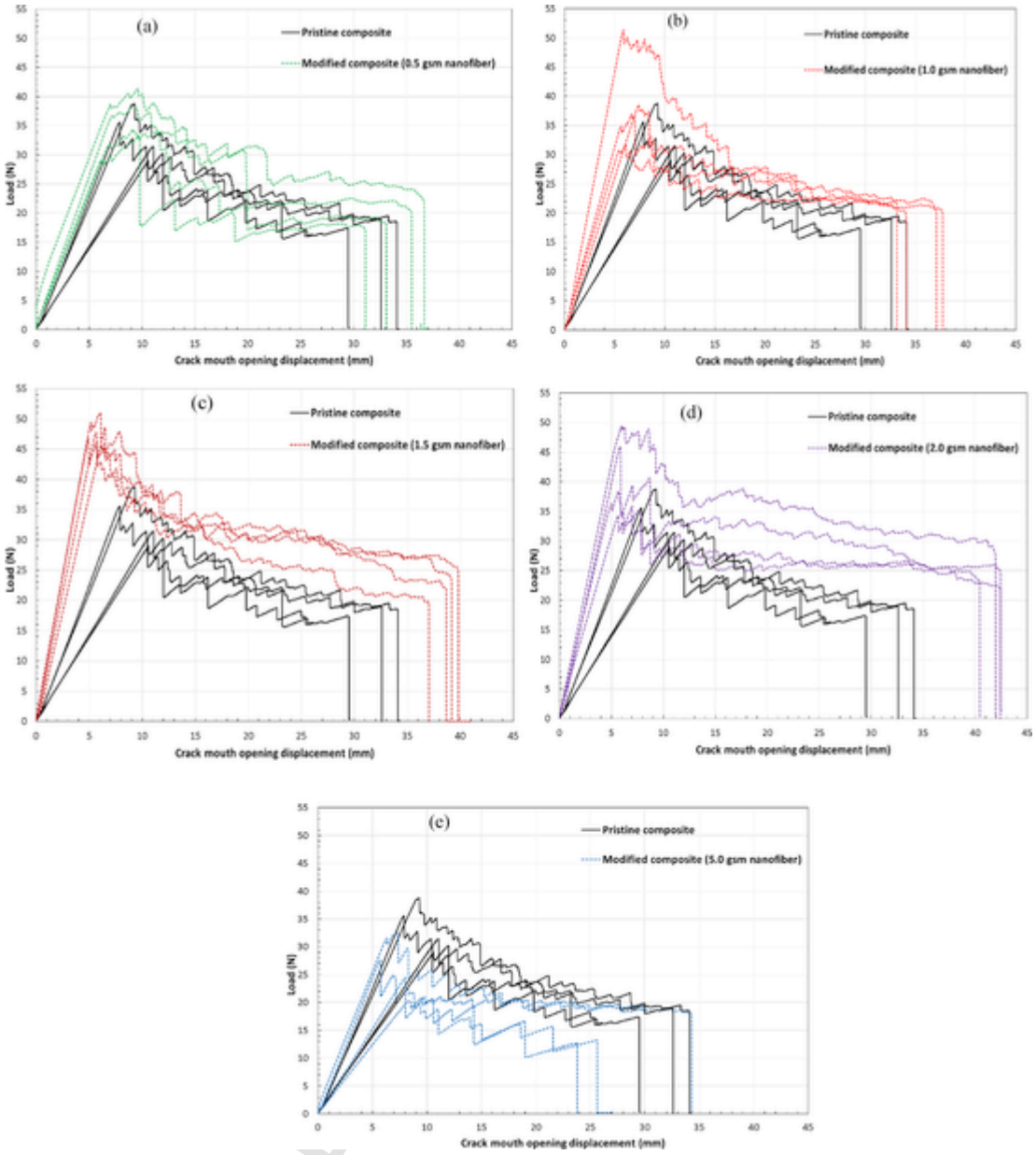

Fig. 6. Comparison of evolution of driven force with crack mouth opening displacement in pristine (non-modified) and modified glass fiber-reinforced phenolic composites with electrospun thermoplastic nanofibers at densities of (a) 0.5 gsm, (b) 1.0 gsm, (c) 1.5 gsm, (d) 2.0 gsm, and (e) 5.0 gsm.

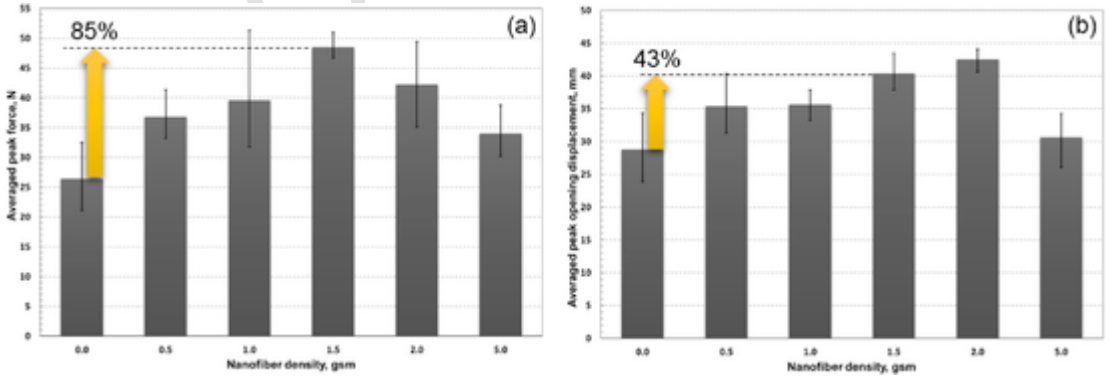

Fig. 7. Comparison of pristine and electrospun nanofiber-modified glass fiber-reinforced phenolic composites at nanofiber densities of 0.5, 1.0, 1.5, 2.0, and 5.0 gsm: (a) averaged maximum load data and (b) averaged maximum crack mouth opening displacement data.

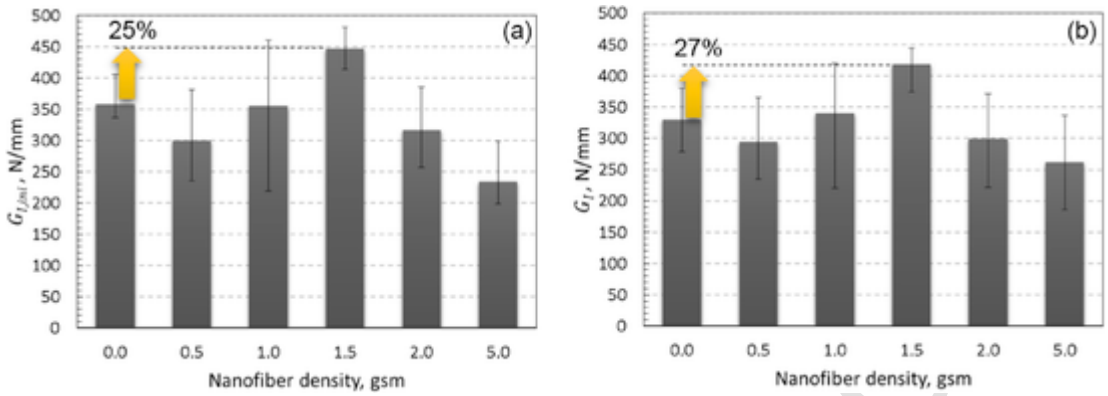

Fig. 8. Evolution of fracture toughness with the increasing electrospun nanofiber density: (a) $G_{I,ini}$ at the initiation stage and (b) G_I at the propagation stage.

In addition, it was observed that the nanofiber-modified specimens exhibited a more stable crack propagation at 1.5 and 2 gsm, and a more unstable instantaneously occurring crack propagation at densities above 2.0 gsm. New mechanisms induced by the nanofibers within the interlayer have also allowed increasing the potential for elastic and plastic yield of the laminate in opening mode during the propagation phase. It may be envisaged that the nanofibers ahead of the tip of a propagating crack effectively dissipate the strain energy via extensive deformation rather than damage, therefore creating a plastic zone ahead of the crack edge tip. Such deformation mechanism, in the subsequent loading, creates bridges between the two neighboring plies, holding the fracture surfaces together and mitigating the creation of new crack faces. The presence of this bridging phenomenon would be a mark of improvement of the resistance to Mode I loads, resulting in greater steps of load increase. To observe such phenomenon at the microscale, fractography using SEM was carried out to support the link between the nanofibers and the variation of fracture toughness.

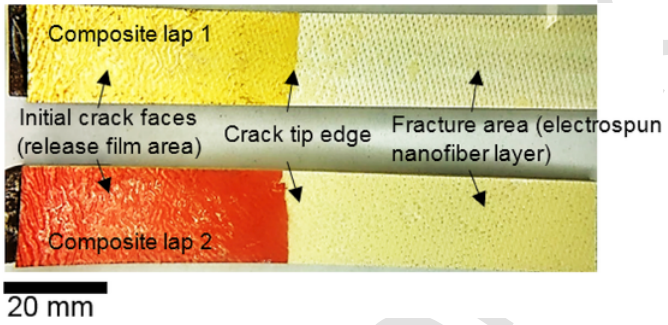

Fig. 9. Crack open DCB specimen laps post failure.

4.1. Microscopy data

To observe a correlation between variation of G_I and nanofiber density, specimens were carefully cut on their crack faces post failure to fit the SEM cavity for microstructural fractography. The dominant mechanism was observed as an interfacial fracture between the composite plies visible in Fig. 9 for a typical modified specimen. Generally in most of the specimens, it was observed that any force drop throughout the test (see-saw drops in Fig. 6) was associated with an instantaneously occurring delamination as opposed to the increase in force levels, due to progressive (gradual) creation of crack faces.

Fig. 10 compares the fracture surfaces in pristine and nanofiber-modified specimens. A closer look on the glass fiber reinforcement reveals a significant distinction on the surfaces morphology: unlike the surface of the reinforcements in the pristine specimen, the glass fibers in the nanofiber-modified specimens exhibit a surface containing numerous pores made of nylon-6,6. Fig. 11 shows the SEM image for glass fiber rich area in a pristine specimen where instantaneously occurred delamination has bared the glass reinforcements off the phenolic matrix. However, for the modified specimens having a nanofiber density of greater than 1.5 gsm, the nanofibers form a barrier for the phenolic resin to flow through and adequately wet the glass fibers, so they have resulted in reduction of peak load and fracture toughness (Figs. 7 and 8). A low wettability of the nanofibers by the resin at high densities results in a weak interface and, therefore, in a preferential path for the crack propagation. In addition to the wettability issue, in an analogous way to high glass fiber volume fraction, the proportion

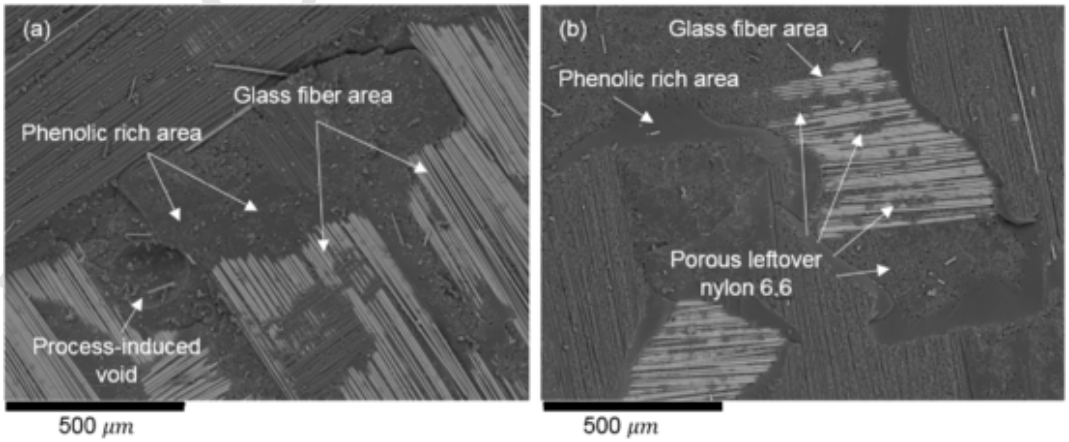

Fig. 10. Comparison of fracture surfaces comprising of glass fiber reinforcements and phenolic matrix in (a) pristine specimen and (b) nanofiber-modified specimen.

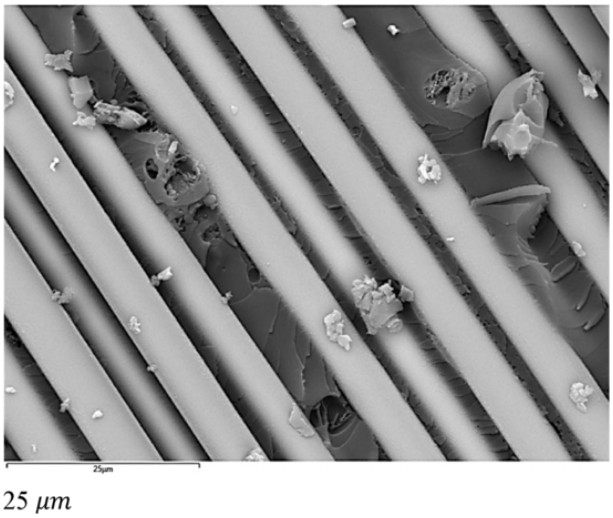

Fig. 11. SEM image of typical DCB pristine specimen at ultimate failure in glass fibers area (Fig. 10(a)).

of nanofibers areal distribution (e.g., 4 gsm) should be considered more carefully. Nanofibers have huge surface area, potentially conferring a strong interface. In case of excessive proportion of nanofibers, the resin becomes soaked up on the fibers, leading to weak bonds between the plies during the co-process. Consequently, delamination becomes very likely to occur in high nanofiber density as well as in low density. We have then taken this extreme case of 4.0 gsm to investigate the performance reduction.

Fig. 12 presents fracture surface images of 5.0 gsm nano-modified specimens that have failed at the lowest load assessed herein with the lowest G_I. The nanofibers are not present in pristine specimens (Fig. 11), and thus no residue of matrix remains stuck to the surface of the fibers, making a smooth surface whereas the electrospun, co-processed nanofibers gather around the fibers and create a spider web-shaped structure. Also, the nanofibers at 4.0 gsm are seen having created a porous and deformable structure; however, owing to the excess of the nanofibers diffused within the phenolic resin during the co-process and covering the glass fibers, chemical disbond is induced between the fibers and the phenolic matrix, a well-known phenomenon (see, e.g., Ref. [43]). The porous structure represents nanoscale fibers that have failed in a brittle manner because no reduction of the cross-section was observed. Such phenomenon is more evident in Fig. 13 in the magnified nanofibers area. A deformation of the ductile matrix would have given a less regular failure.

Generally, by comparing the matrix/fiber interface in the two laminates (pristine and modified), any new bond in the interfacial area would be directly related to the addition of nanofibers, which at densities above 2.0 gsm would create disbond due to excessive diffusion of nanofibers through the matrix and over the reinforcement surface, thus resulting in degradation in load-carrying capacity and fracture response.

5. Conclusions

The manufacturing process of handling pre-pregs electrospun with thermoplastic nanofibers via room temperature electrospinning was carried out on phenolic pre-impregnated glass fiber-reinforced composite plies, followed by a co-process in an autoclave and using vacuum bagging. It was observed that though the nanofibers were ultra-thin and of low-density, apparent improvements in the mechanical performance, damage tolerance, and fracture toughness could be achieved if the density of nanofibers is taken into control. Nanofiber density levels at 0.5, 1.0, 1.5, 2.0, and 4.0 gsm were examined.

The findings for 1.5 gsm demonstrated the most promising and reliable nano-modification for the proposed laminate in coupon test

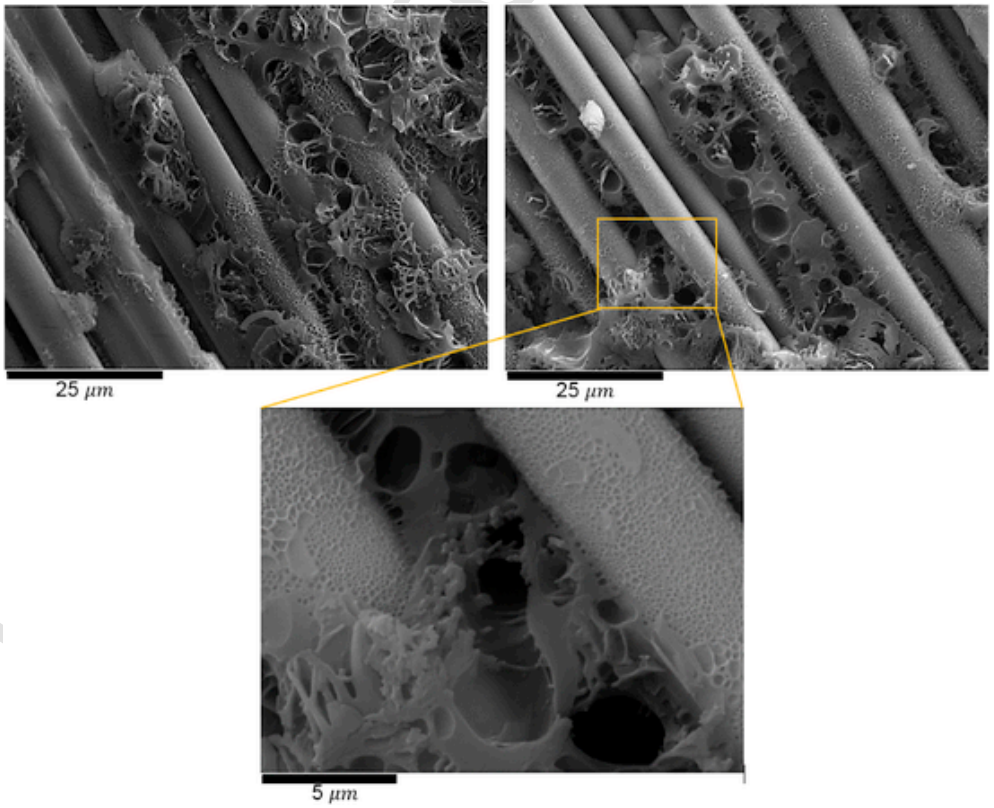

Fig. 12. SEM images of typical DCB nanofiber-modified specimen (5.0 gsm herein) at ultimate failure in glass fibers area (Fig. 10(b)).

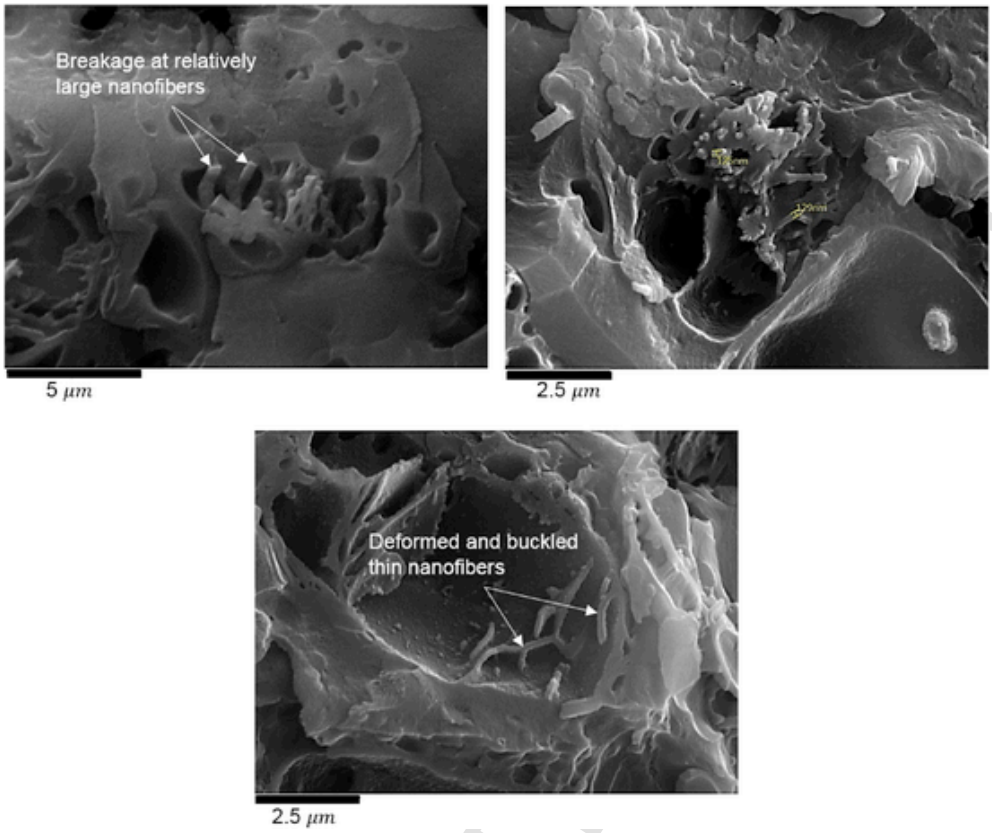

Fig. 13. SEM images showing the presence of deformed and broken nanoscale structures at ultimate failure from different locations, appearing to be electrospun nanofibers at diameters of 100–200 nm.

specimens, via improvements up to 85% and 43% in peak load and crack opening displacement, respectively, with improvement (>25%) of fracture toughness at both initiation and propagation phases, and initial stiffness improvement by nearly 150% in the linear regime prior damage initiation. The stiffening mechanism was observed due to the enhancement of adhesion properties and contribution of deformation mechanisms (plastic zone creation and fiber bridging) at the right density of 1.5 and 2.0 gsm. Excessive electrospun nanofibers (above 2.0 gsm) were found degrading rather than improving the performance, dominantly due to the diffusion of nanofiber onto the glass reinforcements and creation of interfacial defects (disbond). Such conclusion must emphasize that the 1.5 gsm is an optimum nanofiber density for the phenolic resin. Other matrix such as epoxy and polyesters will require similar approach to determine the optimum nanofiber loading.

Acknowledgments

The authors would like to acknowledge the UK Engineering and Physical Sciences Research Council funded projects, STRAINcomp (Ref. No. EP/R016828/1) and CAMREG (Ref. No. EP/P007805/1). The authors would also like to thank Peter Carr, Safran Seats UK for supplying and managing the manufacture of the phenolic panels, and Jim Hurley and Ben Hopper at the Enhanced Composites & Structures Centre at the Cranfield University. The underlying data can be accessed through the Cranfield University repository at https://doi.org/10.17862/cranfield.rd.10058372.

References

[1] J. Schon, T. Nyman, A. Blom, H. Ansell, A numerical and experimental investigation of delamination behaviour in the DCB specimen, Compos. Sci. Technol. 60 (2) (2000) 173–184, doi:10.1016/s0266-3538(99)00113-x.
[2] Y.H. Tang, L. Ye, Z. Zhang, K. Friedrich, Interlaminar fracture toughness and CAI strength of fiber-reinforced composites with nanoparticles - a review, Compos. Sci. Technol. 86 (Sep 2013) 26–37, doi:10.1016/j.compscitech.2013.06.021.
[3] C.S. Lopes, P.P. Camanho, Z. Gurdal, P. Maimi, E.V. Gonzalez, Low-velocity impact damage on dispersed stacking sequence laminates. Part II: numerical simulations, Compos. Sci. Technol. 69 (7–8) (Jun 2009) 937–947, doi:10.1016/j.compscitech.2009.02.015.
[4] H.Y. Nezhad, F. Merwick, R.M. Frizzell, C.T. McCarthy, Numerical analysis of low-velocity rigid-body impact response of composite panels, Int. J. Crashworthiness 20 (1) (Jan 2015) 27–43 in English, doi:10.1080/13588265.2014.963378.
[5] A. Mohammadabadi, R. Dugnani, Design and evaluation of a novel low acoustic impedance-based PZT transducer for detecting the near-surface defects, engrXiv (2019), doi:10.31224/osf.io/u7aby.
[6] A. Mohammadabadi, R. Dugnani, Impact damage detection in fiberglass composites using low acoustic impedance-based PZT transducers, engrXiv (2019), doi:10.31224/osf.io/muj72.
[7] S. Deane, et al., Application of NDT thermographic imaging of aerospace structures, Infrared Phys. Technol. 97 (Mar 2019) 456–466, doi:10.1016/j.infrared.2019.02.002.
[8] A. Sirikham, Y.F. Zhao, H.Y. Nezhad, W.X. Du, R. Roy, Estimation of damage thickness in fiber-reinforced composites using pulsed thermography, IEEE Trans. Ind. Inf 15 (1) (Jan 2019) 445–453, doi:10.1109/tii.2018.2878758.
[9] H. Yazdani Nezhad, D. Stratakis, D. Ayre, S. Addepalli, Y. Zhao, Mechanical performance of composite bonded joints in the presence of localised process-induced zero-thickness defects, Procedia Manuf. 16 (2018) 91–98, doi:10.1016/j.promfg.2018.10.175.
[10] E.V. Gonzalez, P. Maimi, P.P. Camanho, A. Turon, J.A. Mayugo, Simulation of drop-weight impact and compression after impact tests on composite laminates, Compos. Struct. 94 (11) (Nov 2012) 3364–3378, doi:10.1016/j.compstruct.2012.05.015.
[11] H. Zabala, L. Aretxabaleta, G. Castillo, J. Urien, J. Aurrekoetxea, Impact velocity effect on the delamination of woven carbon-epoxy plates subjected to low-velocity equienergetic impact loads, Compos. Sci. Technol. 94 (Apr 2014) 48–53, doi:10.1016/j.compscitech.2014.01.016.
[12] R. Bhanushali, D. Ayre, H.Y. Nezhad, Tensile response of adhesively bonded composite-to-composite single-lap joints in the presence of bond deficiency, in:

R. Roy, Proceedings of the 5th International Conference in Through-Life Engineering Services, 59, Procedia CIRP, 2017, pp. 139–143.
[13] H.Y. Nezhad, Y.F. Zhao, P.D. Liddel, M.A. Veronica, R. Roy, A novel process-linked assembly failure model for adhesively bonded composite structures, CIRP Ann. - Manuf. Technol. 66 (1) (2017) 29–32, doi:10.1016/j.cirp.2017.04.103.
[14] Y. Liu, X. Zhang, S. Lemanski, H. Yazdani Nezhad, D. Ayre, Experimental and numerical study of process-induced defects and their effect on fatigue debonding in composite joints, Int. J. Fatigue 125 (2019) 47–57.
[15] Y.D. Liu, S. Lemanski, X. Zhang, D. Ayre, H.Y. Nezhad, A finite element study of fatigue crack propagation in single lap bonded joint with process-induced disbond, Int. J. Adhesion Adhes. 87 (Dec 2018) 164–172, doi:10.1016/j.ijadhadh.2018.10.005.
[16] Y. L, L. S, Z. X, A. D, Y.N. H, Finite element study on the static and fatigue behaviour of wide single lap bonded joints with semi-circular defect, 2018.
[17] Y.N. H, A. V, M. CT, O.H. RM, Impact damage response of carbon fiber-reinforced aerospace composite panels, 2015 [Online]. Available:, doi:10.13140/RG.2.1.2174.4081. http://www.iccm-central.org/Proceedings/ICCM20proceedings/.
[18] E. Fuoss, P.V. Straznicky, C. Poon, Effects of stacking sequence on the impact resistance in composite laminates - Part 1: parametric study, Compos. Struct. 41 (1) (Jan 1998) 67–77, doi:10.1016/s0263-8223(98)00036-1.
[19] Y.N. H, T. VJ, Effect of morphological changes due to increasing carbon nanoparticles content on the quasi-static mechanical response of epoxy resin, Polymers 2018 (2018), doi:10.3390/polym10101106.
[20] S. Lotfian, C. Giraudmaillet, A. Yoosefinejad, V.K. Thakur, H.Y. Nezhad, Electrospun piezoelectric polymer nanofiber layers for enabling in situ measurement in high-performance composite laminates, ACS Omega 3 (8) (Aug 2018) 8891–8902, doi:10.1021/acsomega.8b00940.
[21] Y.N. H, T. VK, G. C, P. R, Y. A, Electrospun piezoelectric thermoplastic nanofibre layers for toughening and in-situ measurement of laminated composites, 2018 [Online]. Available:. http://www.ecnf2018.org/pdf/abstract-program.pdf.
[22] W.L. Zang, Y.X. Nie, D. Zhu, P. Deng, L.L. Xing, X.Y. Xue, Core-shell In2O3/ZnO nanoarray nanogenerator as a self-powered active gas sensor with high H2S sensitivity and selectivity at room temperature, J. Phys. Chem. C 118 (17) (May 2014) 9209–9216, doi:10.1021/jp500516t.
[23] X.Y. Xue, et al., CuO/PVDF nanocomposite anode for a piezo-driven self-charging lithium battery, Energy Environ. Sci. 6 (9) (Sep 2013) 2615–2620, doi:10.1039/c3ee41648h.
[24] D. Zhu, Y.M. Fu, W.L. Zang, Y.Y. Zhao, L.L. Xing, X.Y. Xue, Piezo/active humidity sensing of CeO2/ZnO and SnO2/ZnO nanoarray nanogenerators with high response and large detecting range, Sens. Actuators B Chem. 205 (Dec 2014) 12–19, doi:10.1016/j.snb.2014.08.060.
[25] L.L. Xing, Y.X. Nie, X.Y. Xue, Y. Zhang, PVDF mesoporous nanostructures as the piezo-separator for a self-charging power cell, Nano Energy 10 (Nov 2014) 44–52, doi:10.1016/j.nanoen.2014.09.004.
[26] T.T. Zhao, et al., An infrared-driven flexible pyroelectric generator for non-contact energy harvester, Nanoscale 8 (15) (2016) 8111–8117, doi:10.1039/c5nr09290f.
[27] Y.J. Lin, et al., Room-temperature self-powered ethanol sensing of a Pd/ZnO nanoarray nanogenerator driven by human finger movement, Nanoscale 6 (9) (2014) 4604–4610, doi:10.1039/c3nr06809a.
[28] X.P. Zhuang, K.F. Jia, B.W. Cheng, K.T. Guan, W.M. Kang, Y.L. Ren, Preparation of polyacrylonitrile nanofibers by solution blowing process, J. Eng. Fibers Fabr. 8 (1) (2013) 88–93.
[29] A. Nasajpour, et al., Nanostructured fibrous membranes with rose spike-like architecture, Nano Lett. 17 (10) (Oct 2017) 6235–6240, doi:10.1021/acs.nanolett.7b02929.
[30] A. Nasajpour, et al., A multifunctional polymeric periodontal membrane with osteogenic and antibacterial characteristics, Adv. Funct. Mater. 28 (3) (Jan 17 2018), doi:10.1002/adfm.201703437 1703437.
[31] P. Akangah, S. Lingaiah, K. Shivakumar, Effect of Nylon-66 nano-fiber interleaving on impact damage resistance of epoxy/carbon fiber composite laminates, Compos. Struct. 92 (6) (May 2010) 1432–1439, doi:10.1016/j.compstruct.2009.11.009.
[32] K. Shivakumar, S. Lingaiah, H.C. Chen, P. Akangah, G. Swaminathan, L. Russell, Polymer nanofabric interleaved composite laminates, AIAA J. 47 (7) (Jul 2009) 1723–1729, doi:10.2514/1.41791.
[33] R. Palazzetti, et al., Influence of electrospun Nylon 6,6 nanofibrous mats on the interlaminar properties of Gr-epoxy composite laminates, Compos. Struct. 94 (2) (Jan 2012) 571–579, doi:10.1016/j.compstruct.2011.08.019.
[34] H. Saghafi, A. Zucchelli, R. Palazzetti, G. Minak, The effect of interleaved composite nanofibrous mats on delamination behavior of polymeric composite materials, Compos. Struct. 109 (Mar 2014) 41–47, doi:10.1016/j.compstruct.2013.10.039.
[35] T.M. Brugo, G. Minak, A. Zucchelli, H. Saghafi, M. Fotouhi, An investigation on the fatigue based delamination of woven carbon-epoxy composite laminates reinforced with polyamide nano fibers, Xxiii Italian Group of Fracture Meeting, 109, 2015, pp. 65–72 Igfxxiii, doi:10.1016/j.proeng.2015.06.208.
[36] T. Brugo, et al., Study on Mode I fatigue behaviour of Nylon 6,6 nanoreinforced CFRP laminates, Compos. Struct. 164 (Mar 2017) 51–57, doi:10.1016/j.compstruct.2016.12.070.
[37] T. Brugo, R. Palazzetti, The effect of thickness of Nylon 6,6 nanofibrous mat on Modes I-II fracture mechanics of UD and woven composite laminates, Compos. Struct. 154 (Oct 2016) 172–178, doi:10.1016/j.compstruct.2016.07.034.
[38] J. Zhang, T. Yang, T. Lin, C.H. Wang, Phase morphology of nanofibre interlayers: critical factor for toughening carbon/epoxy composites, Compos. Sci. Technol. 72 (2) (Jan 2012) 256–262, doi:10.1016/j.compscitech.2011.11.010.
[39] Y.A. Dzenis, D.H. Reneker, Delamination Resistant Composites Prepared by Small Diameter Fiber Reinforcement at Ply Interfaces, 2001.
[40] X.F. Wu, A.L. Yarin, Recent progress in interfacial toughening and damage self-healing of polymer composites based on electrospun and solution-blown nanofibers: an overview, J. Appl. Polym. Sci. 130 (4) (Nov 2013) 2225–2237, doi:10.1002/app.39282.
[41] Y. Dzenis, Materials science - structural nanocomposites, Science 319 (5862) (Jan 2008) 419–420, doi:10.1126/science.1151434.
[42] ASTM 5528, Standard Test Method for Mode I Interlaminar Fracture Toughness of Unidirectional Fiber-Reinforced Polymer Matrix Composites, ASTM, 2007.
[43] J.B. Shortall, H.W.C. Yip, Effect of surface treatments on the interfacial bond strength in glass fiber-polyester resin systems, J. Adhes. 8 (2) (1976) 155–169.